Numerical study of transition to supersonic flows in the edge plasma

Rajiv Goswami, Jean-François Artaud, Frédéric Imbeaux, and Predhiman Kaw

---

Articles you may be interested in

Boundary conditions for plasma fluid models at the magnetic presheath entrance
Phys. Plasmas **19**, 122307 (2012); 10.1063/1.4771573

Numerical investigation of edge plasma phenomena in an enhanced D-alpha discharge at Alcator C-Mod: Parallel heat flux and quasi-coherent edge oscillations
Phys. Plasmas **19**, 082311 (2012); 10.1063/1.4747503

Free-boundary magnetohydrodynamic equilibria with flow
Phys. Plasmas **18**, 022502 (2011); 10.1063/1.3551714

Flow and shear behavior in the edge and scrape-off layer of L-mode plasmas in National Spherical Torus Experiment
Phys. Plasmas **18**, 012502 (2011); 10.1063/1.3533435

Fluid-particle hybrid simulation on the transports of plasma, recycling neutrals, and carbon impurities in the Korea Superconducting Tokamak Advanced Research divertor region
Phys. Plasmas **12**, 062504 (2005); 10.1063/1.1914807

Numerical study of transition to supersonic flows in the edge plasma

Rajiv Goswami,[1,a)] Jean-François Artaud,[1] Frédéric Imbeaux,[1] and Predhiman Kaw[2]

[1]*CEA, IRFM, F-13108 Saint-Paul-lez-Durance, France*
[2]*Institute for Plasma Research, Bhat, Gandhinagar—382428, India*

The plasma scrape-off layer (SOL) in a tokamak is characterized by ion flow down a long narrow flux tube terminating on a solid surface. The ion flow velocity along a magnetic field line can be equal to or greater than sonic at the entrance of a Debye sheath or upstream in the presheath. This paper presents a numerical study of the transition between subsonic and supersonics flows. A quasineutral one-dimensional (1D) fluid code has been used for modeling of plasma transport in the SOL along magnetic field lines, both in steady state and under transient conditions. The model uses coupled equations for continuity, momentum, and energy balance with ionization, radiation, charge exchange, and recombination processes. The recycled neutrals are described in the diffusion approximation. Standard Bohm sheath criterion is used as boundary conditions at the material surface. Three conditions conducive for the generation of supersonic flows in SOL plasmas have been explored. It is found that in steady state high (attached) and low (detached) divertor temperatures cases, the role of particle, momentum, and energy loss is critical. For attached case, the appearance of shock waves in the divertor region if the incoming plasma flow is supersonic and its effect on impurity retention is presented. In the third case, plasma expansion along the magnetic field can yield time-dependent supersonic solutions in the quasineutral rarefaction wave. Such situations can arise in the parallel transport of intermittent structures such as blobs and edge localized mode filaments along field lines. © *2014 AIP Publishing LLC*.
[http://dx.doi.org/10.1063/1.4890026]

I. INTRODUCTION AND MOTIVATION

The plasma flow on the open field lines that surround a magnetically confined plasma volume consists of flow components aligned along and across magnetic field lines. It has become clear in recent years that these scrape-off layer (SOL) flows can play important roles in a reactor, such as, affecting SOL impurity transport and screening from the confined plasma,[1] influencing the balance of material erosion and re-deposition between inner and outer divertor legs,[2] imposing a toroidal rotation boundary condition on the confined plasma that depends on flux surface topology, to possibly explaining the dependence of the L-H power threshold on X-point location in a tokamak.[3] Understanding the complex SOL flow patterns may then permit development of mitigation techniques for tritium accumulation, mitigating divertor target heat loads and divertor pumping to control core density. Fast parallel flows thus appear to have a number of important practical implications for magnetic fusion devices. Flows due to plasma expansion are also believed to play an important role in diverse areas, such as edge localized mode (ELM) filaments,[4] laser-plasma interaction, refuelling by pellet ablation,[5] polar wind,[6] electromagnetic propulsion methods, plasma processing, etc. The motivation for improved understanding and modelling is therefore strong.

It has been observed in the SOL of many tokamaks that the plasma flow velocities along magnetic field lines

approach a significant fraction of the local sound speed.[7] Evidence for such near-sonic parallel flows also exists in the far SOL of limiter tokamaks.[8] High Mach flow associated with X-point MARFE have also been observed in two dimensional (2D) simulations.[9] Such large flows, though expected close to a material surface, are found in regions far away from any surface, for example, in the inboard midplane far SOL in C-Mod.[10] They arise in response to poloidal transport asymmetries and are independent of the sign of the magnetic field (**B**), in contrast to those boundary layer flows, which depend on the sign of **B** and therefore change with field direction.[11] Strong parallel flows have also been observed in the SOL of ASDEX Upgrade, with Mach numbers even larger than 1 above the divertor.[12] These observations thus elicit the possibility of large parallel flows undergoing a transition from subsonic to supersonic state. Such an outcome has been predicted earlier in the context of topside ionosphere,[13] the Bohm-Chodura sheath criterion,[14] detached plasmas,[15,16] etc. However, in a recent paper, Ghendrih *et al.*[17] have proposed that with a single dimensionless control parameter $\mathcal{A}$, such a transition could be described as a bifurcation. The bifurcation point is then characterized by some specific properties of this control parameter $\mathcal{A}$, which is the ratio of the particle flux times the acoustic velocity divided by the total momentum flux.

In this paper, we present a numerical study of transition to supersonic flows in a quasineutral plasma of the SOL. In particular, our aim is to also elucidate and corroborate the role of the control parameter $\mathcal{A}$ and its various constituents. Since the physics in this region of tokamaks is very intricate involving many atomic physics processes and geometrical

---

a)Author to whom correspondence should be addressed. Permanent Address: Institute for Plasma Research, Bhat, Gandhinagar - 382428, India. Electronic address: rajiv@ipr.res.in

effects, it is difficult to construct reasonably simple mathematical models for the SOL plasma. Large, multifluid, 2D plasma codes such as SOLPS[18] and UEDGE[19] coupled to Monte Carlo/fluid codes for neutral species, e.g., EIRENE/NIMBUS[20,21] have been developed to investigate such problems. However, to gain physical insight and extricate qualitatively useful information, as a good first approximation, a one-dimensional treatment describing the direction parallel to the field lines is often used, because transport along field lines is large even with anomalous radial transport. Although the neglected 2D effects also give rise to boundary flows due to cross-field $E_r \times B$ and diamagnetic drifts, and neoclassical Pfirsch-Schlüter flows, which can add or cancel the parallel flows depending on the direction of $\mathbf{B} \times \nabla B$ relative to the X-point, it is the low-field-side (LFS) radial fluctuation-induced particle fluxes which act as primary driver for the high velocity along the magnetic field lines flows seen on the high-field-side (HFS) of tokamaks.[11]

We have thus carried out our study using the complete set of coupled, nonlinear, 1D fluid equations, with realistic sheath boundary conditions at divertor target. In this paper, as against many theoretical models, we have included the energy transport equations. Specifically, we have also used the ion energy transport equation, as the equal temperature assumption used in other 1D modelling is questionable, because apart from the ions and electrons having quite different source/sink terms, their very different masses can produce a tendency to thermally decouple. Our simulation results match and confirm the theoretical arguments presented in Ref. 17, while allowing a more comprehensive numerical study of the role of various parameters. The other motivation for a 1D SOL model is its possible application to an integrated modelling of core-edge coupling, taking advantage of a drastic reduction in computation time compared to the comprehensive 2D models. Our numerical code SOL1D has been thus coupled to the CRONOS suite of codes,[22] a work that will be presented in a separate paper.

The plan of the paper is as follows: In Sec. II, the physical model used for the numerical simulation is presented. In Sec. III, we present the various results of the simulation. In particular, we investigate the three means of attaining supersonic transition in a quasineutral plasma, namely, a low temperature detached plasma state, a low divertor density and high temperature "attached" regime, and the expansion of a hot dense plasma against a lower-density background. The detached state can be reached through the traditional route of losing ion momentum through copious collisions with recycled neutrals and electron energy loss by impurity radiation. The sonic transition is found to occur very close to the target. The attached case is found to require very low values of target recycling coefficient, as opposed to the detached case. It also depends on the ratio of the volumetric density of cross-field energy and particle sources. For intermediate values of recycling coefficient, stationary shock solutions in the divertor region are obtained, which can be helpful in impurity control. Here, the sonic point location is always closer to the X-point. In the third regime, large parallel flows are found to be generated during the radial transport of initially nonuniform (along the magnetic field $\mathbf{B}$) blob and

ELM filaments.[23] Parallel transport of these intermittent events may be important to divertor design, since ion energies directed into the divertor plate may be greater during such a transient than at steady state. Moreover, it can also yield information about the time required for a blob-filament from its release to dump its energy on the target, which could be useful for its active cooling. These flows can also display the onset of interesting transient nonlinear phenomena such as rarefaction and unsteady shock waves in the SOL. Finally, in Sec. IV, our conclusions are summarized.

II. NUMERICAL MODEL

The SOL is assumed in a slab geometry. A schematic representation is shown in Fig. 1. The arc length, x, along the field lines from the stagnation point ($x = 0$) to the target plates ($x = x_t$) is used as the spatial coordinate. Since the SOL plasma is in contact with the confined plasma volume from $x = 0$ to the X-point ($x = x_x$), the particle and heat fluxes from the plasma core enter into this line segment of the SOL as cross-field sources and reach the divertor along open field lines, where they are convected through the sheath at the target plate. Assuming charge neutrality $n_e = n_i = n$ and ambipolarity $v_e = v_i = v$ (no net parallel current $j_\parallel = 0$), the variation of the plasma density n, parallel velocity v, electron temperature T_e, and ion temperature T_i is described by

$$\frac{\partial n}{\partial t} + \frac{\partial}{\partial x}(nv) = S_\perp \theta(x_x - x) + nn_n\langle\sigma v\rangle_i - n^2\langle\sigma v\rangle_r, \quad (1)$$

$$\frac{\partial}{\partial t}(m_i nv) + \frac{\partial}{\partial x}(m_i nv^2)$$
$$= -\frac{\partial}{\partial x}(p_e + p_i) - m_i nv(n_n\langle\sigma v\rangle_{cx} + n\langle\sigma v\rangle_r), \quad (2)$$
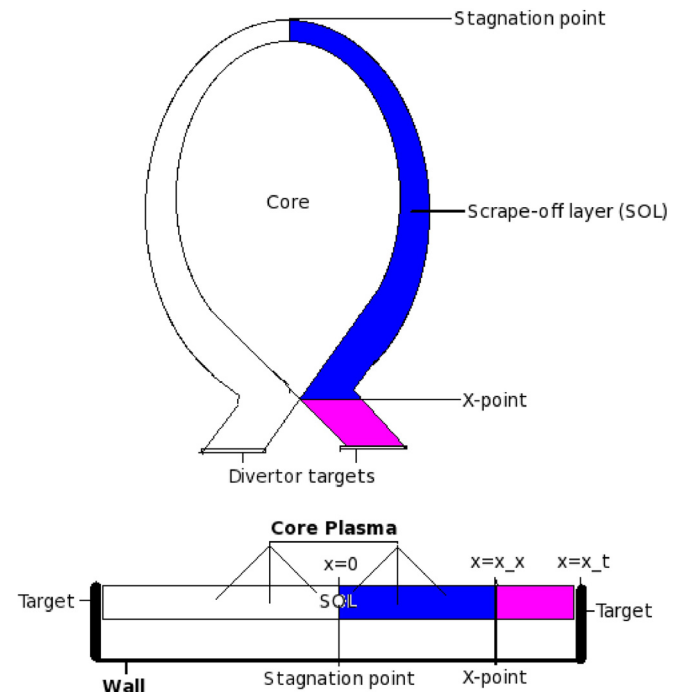

FIG. 1. Schematic of the simulation setup and domain.

$$\frac{\partial}{\partial t}\left(\frac{3}{2}nT_e\right) + \frac{\partial}{\partial x}\left(\frac{5}{2}nvT_e - \kappa_{\parallel e}\frac{\partial T_e}{\partial x}\right)$$

$$= Q_{\perp e}\theta(x_x - x) + v\frac{\partial p_e}{\partial x} - n\nu_{ei}(T_e - T_i)$$

$$- nn_n\langle\sigma v\rangle_i E_i - \frac{3}{2}T_e n^2\langle\sigma v\rangle_r - n^2\xi_I L_z(T_e), \qquad (3)$$

$$\frac{\partial}{\partial t}\left(\frac{3}{2}nT_i + \frac{1}{2}m_i nv^2\right) + \frac{\partial}{\partial x}\left(\frac{5}{2}nvT_i + \frac{1}{2}m_i nv^3 - \kappa_{\parallel i}\frac{\partial T_i}{\partial x}\right)$$

$$= Q_{\perp i}\theta(x_x - x) - v\frac{\partial p_e}{\partial x} + n\nu_{ei}(T_e - T_i)$$

$$- \left[\frac{3}{2}T_i + \frac{1}{2}m_i v^2\right]\left(nn_n\langle\sigma v\rangle_{cx} + n^2\langle\sigma v\rangle_r\right), \qquad (4)$$

where m_i is the ion mass, n_n and T_n are the recycling neutral density and temperature, p_i and p_e are the ion and electron static pressure, $\langle\sigma v\rangle_i$, $\langle\sigma v\rangle_r$, and $\langle\sigma v\rangle_{cx}$ are the Maxwellian averaged electron impact ionization, recombination, and charge exchange rate coefficients, and E_i is the energy loss of electrons due to excitation and ionization of neutral atoms. The $\kappa_{\parallel e(i)}$ and ν_{ei} are the electron(ion) parallel thermal conductivities, and thermal equipartition coefficients, respectively. The transport coefficients are classical and do not include the flux limits in order to account for kinetic effects, which are important when the scale length of the variation of plasma parameters along the field is comparable to the relevant mean free paths. However, note that the value of heat flux limiters is sensitive to the collisionality; and since there is a lack of systematic study of kinetic corrections and their parametrization with plasma parameters,[24] the heat flux here is prescribed by the classical Spitzer-Härm expression. The radiation loss is taken to be a fixed fraction (ξ_I) of the ion density, along with a coronal equilibrium model for calculating the radiation losses due to carbon impurities. Although this simple impurity model does not provide information on the impurity distribution, it does retain a feature that is essential for detachment, namely a strong reduction of the heat flux through line radiation. The function $\theta(x)$ is the Heaviside step function, with $S_\perp$ and $Q_{\perp e(i)}$ being the uniformly distributed perpendicular sources of particles and heat into the SOL from the core, respectively. It is further assumed that the radial outflow of plasma does not contribute to the parallel momentum in Eq. (2). We have ignored the effect of magnetic field variations and hence the mirror force, which is proportional to $\nabla_\parallel B/B$. This force, which acts as magnetic flux expansion source term in these equations, plays a larger role in the SOL modelling of low aspect ratio devices such as spherical tokamak.

The energy and particles after being radially transported into the edge region, flow rapidly along the open field lines. The energy gets deposited on the divertor target plates, and the plasma ions after being neutralized diffuse back into the plasma as atoms or molecules. The plasma model is then coupled with a one-dimensional fluid diffusion model of neutrals.[25,26] Although a proper treatment of the neutral dynamics requires Monte Carlo simulations,[20] such a description though more accurate and preferable, is not highly relevant in our present analysis. Note that in case of dense divertor plasmas with very high neutral densities ($\sim 10^{21}$ m^{-3}), a Navier-Stokes kind of neutral transport may have to be employed.[27] We assume that the recycling neutrals, which are emitted from the target plate, diffuse across the background plasma through an ionization and charge exchange mediated process. Due to the dominant charge exchange process, the neutrals are assumed to be in a local thermal equilibrium with the ions, and so $T_n = T_i$ everywhere in the SOL. Ignoring the parallel velocity of neutrals compared to the ion speed v, the diffusion equation for neutral density is then given by

$$\frac{\partial n_n}{\partial t} - \frac{\partial}{\partial z}\left(D_n\frac{\partial n_n}{\partial z}\right) = -nn_n\langle\sigma v\rangle_i + n^2\langle\sigma v\rangle_r, \qquad (5)$$

where $z = (x_t - x)\sin\alpha$ is the length of the magnetic field line projected onto the poloidal plane, and α is the angle at which a magnetic field line intersects the target plate. The diffusion coefficient D_n is

$$D_n = \frac{T_i}{m_i n\left(\langle\sigma v\rangle_i + \langle\sigma v\rangle_{cx}\right)}. \qquad (6)$$

The boundary conditions for Eqs. (1)–(5) are imposed by the symmetry of the system at the stagnation point $x = 0$

$$M = \frac{dn}{dx} = \frac{dn_n}{dz} = \frac{dT_{e(i)}}{dx} = 0, \qquad (7)$$

where $M = v/c_s$ is the Mach number, with $c_s = \sqrt{(T_e + T_i)/m_i}$ as the local isothermal ion sound speed. While the required boundary conditions at the target plates are subject to a considerable degree of uncertainty (due to the transition from a fluid description to a kinetic description of the flow), we have used the standard Bohm criterion to provide the boundary condition for the Mach number,

$$M_t \geq 1. \qquad (8)$$

Usually only the lower limit of M_t is generally assumed in the plasma fluid models. It must be noted that the value of $M_t \geq 1$ evolves without being forced to any specified value. However, if the Mach number at the target is less than one, $M_t = 1$ is forced. Equation (8) thus includes the possibility that the flow could become supersonic at some location upstream of the target. The continuity of electron and ion heat fluxes at the sheath entrance yields the following nonlinear boundary conditions for temperatures T_e and T_i:

$$q_e^c + \frac{5}{2}nvT_e = \gamma_e nvT_e,$$
$$q_i^c + \frac{5}{2}nvT_i + \frac{1}{2}m_i nv^3 = \gamma_i nvT_i, \qquad (9)$$

where q_e^c and q_i^c are parallel electron and ion heat conduction fluxes, $\gamma_e = 5$ and $\gamma_i = 2.5 + M_t^2$ are the typical electron and ion energy transmission coefficients of the sheath. In the present simulations, we have neglected the impact of secondary electron emission from the target plates on these coefficients. The flux of the neutral particles, generated at the target plates by recycling of the plasma ions, follow the condition $\Gamma_n = -R_t\Gamma_i$, with the recycling coefficient $R_t \lesssim 1$.

This system of nonlinear Eqs. (1)–(5) subject to the boundary conditions (7)–(9) is solved using a numerical scheme based on the finite difference method. To utilise the advantage of large gradients forming near the target plates, we use a nonuniform grid to discretize these equations. The grid refinement increases towards the target $x = L$. The advective terms are discretized using a conservative upwind method which captures the essential physical transport property of supersonic flow that advected quantities directly influence the solution only downstream.[28] To ensure positivity, a flux-limiting procedure is also utilised. The diffusive terms are discretized using second-order central differences. The resulting system of discrete equations is solved simultaneously using a globally convergent Newton's method. For transient simulations, we follow the method-of-lines approach, which means that the spatial discretization and temporal integration are considered separately. This approach can be used to find steady-state solutions directly or to follow transients. We checked that the results, as presented in Sec. III, are grid independent. Further details about the numerical scheme will be published elsewhere.[29] Note that instead of quantitative and detailed comparisons with the experimental results, this work will focus more on the essential features and basic characteristics of the phenomena under consideration.

III. COMPUTATIONAL RESULTS

Results are presented for a problem that approximates one half of a single null divertor with geometry scale lengths close to a typical tokamak divertor. In our simulations, nominal ITER-like plasma parameters were assumed.[30,31] The distance L from the stagnation point ($x = 0$) to the divertor target (x_t) is taken to be equal to 100 m, the X-point is set at $x_x = 67$ m, and the pitch angle of the magnetic field $\alpha = 2.5°$. For evaluating the volumetric power $Q_{\perp e(i)}$ and particle source $S_\perp$, the SOL volume can be calculated as $V_{SOL} \equiv 2L \times A_{SOL}$, where $A_{SOL} = 4\pi R \lambda_{q(n)}\left(\frac{B_\theta}{B_\phi}\right)$ and $L \approx \pi R q$. Here, R is the tokamak major radius, $\frac{B_\theta}{B_\phi}$ the magnetic field line pitch angle, q is the safety factor, and $\lambda_{q(n)}$ are the SOL power and particle widths. If P_{SOL} is power crossing the separatrix, then typical volumetric power $Q_{\perp e(i)} = P_{SOL}/V_{SOL}$ and particle inputs $S_\perp = \Gamma_i/V_{SOL}$ from the core to the SOL can range from $(1–5) \times 10^6$ W m^{-3} and $(1–8) \times 10^{22}$ m^{-3} s^{-1}, respectively. Comparing simulated upstream n_e and $T_{e(i)}$ values to expected values can also validate the magnitude of cross-field sources. For simplicity, we have assumed that the power P_{SOL} is divided equally between the electron and ion channels. All lengths and velocities are normalized to the system length L and the velocity v_{T_0}, respectively, where $v_{T_0} = \sqrt{T_0/m_i}$, and $T_0 \simeq (Q_{\perp e} + Q_{\perp i})/[(\gamma_e + \gamma_i)S_\perp]$ eV.

By carrying out the simulation with different values of $S_\perp$ and $Q_{\perp e(i)}$, the change in plasma parameters are observed from the detached states to the attached states. The detached plasma is characterized primarily by low temperatures $\lesssim 1$ eV, resulting in a neutral density build-up due to diminished ionization capability, loss of plasma momentum by charge exchange with the recycled neutrals, and increased

volumetric recombination leading to ion flux reduction. The attached plasma, which may be subdivided into the sheath-limited or low recycling regime and the conduction-limited or high recycling regime, has, apart from other features, relatively high target temperatures with $T^t_{e(i)} \gtrsim 10$ eV. For further details, see Ref. 32.

A. Detached

First, we present stationary solution for a detached case in Fig. 2 and explore the possibility of achieving a supersonic transition on or before the target plates. The simulation result has been obtained by taking $Q_{\perp e(i)}$ as 1.3×10^6 W m^{-3}, with $S_\perp$ corresponding to a value of 5×10^{22} m^{-3} s^{-1}. Carbon is assumed to be the typical impurity with a fraction $\xi_I = 0.05$, and the target recycling coefficient $R_t = 0.99$. Assuming that approximately 90% of input power flows across the separatrix into the SOL, the rest being lost via radiation in the core, we obtain Q_{in} for the detached case studied to be ~ 35 MW, which is in the range of power injected. The vertical dotted lines at $x = 67$ m represent X-point location where the particle and heat source distribution ends. We observe in Figs. 2(a) and 2(e) that though n at the target decreases significantly and the particle flux Γ rolls over, its reduction after the rollover is not very significant. This behaviour has also been reported in detachment modelling using the SONIC suite of divertor codes[33] and was attributed to occurrence of supersonic flow very close to the target. However, note that a substantial reduction in $q_{e+i}^{cnd+cnv}$, the total (conductive and convective) heat fluxes for ions and electrons is obtained, as shown in Fig. 2(f). In the present simulations, we also find that the transition to supersonic flow occurs just in front of the target plates [Fig. 2(b)], in agreement with previous theoretical arguments.[34]

It has been argued that a temperature gradient accelerates the plasma flow from the stagnation point towards the target; and if this gradient is strong enough, the value $M = 1$ can be achieved before the target.[16,17,32,35] In a different analysis,[34] it was observed that the location of the ionization front characterizes a bifurcation, which in turn is associated with the subsonic and supersonic branch of Mach number. In the subsonic regime, along with an increase in the neutral density, the cold and dense plasma ingresses upstream,[36] which may lead to formation of the undesirable X-point MARFE.[37] In case of supersonic flow, alongside the increase in neutral density, the ionization front instead moves towards the target plates. It has also been postulated that regardless of subsonic or supersonic regimes, processes such as friction, addition of particles, viscosity, etc., take M towards the sonic point, whereas, processes such as decrease of temperature move M away from unity.[38]

Thus for a better understanding of the physical phenomena involved, a brief description combining the analytical approaches for treatment of parallel flows in the SOL developed in Refs. 16, 17, and 35 will be given here. We begin by introducing the dimensionless control parameter $\mathcal{A}$,

$$\frac{2M}{1+M^2} = \mathcal{A} = \frac{2m_i \Gamma c_s}{\Pi} \equiv \frac{2M_t G_p(x)}{1+M_t^2 G_m(x)} \times \sqrt{\frac{T_e(x) + T_i(x)}{T_{et} + T_{it}}}, \quad (10)$$
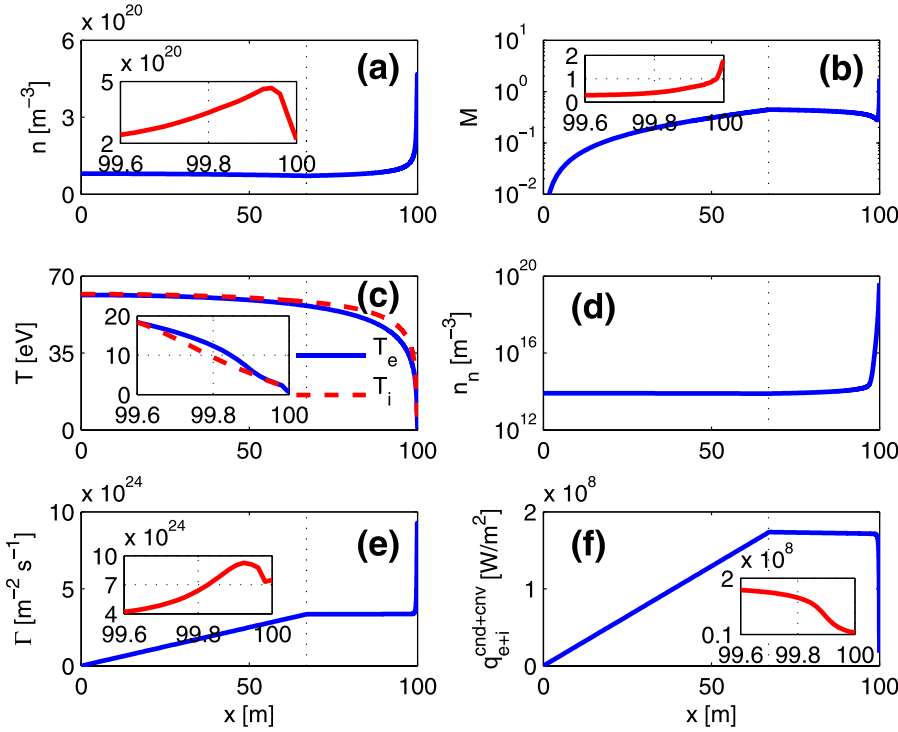
FIG. 2. Numerical profiles of plasma density, Mach number, electron and ion temperature, neutral density, plasma particle flux, and electron and ion total (conductive + convective) heat flux. Here, a high density detached case is shown. Dotted vertical lines represent the X-point location. Inset figures in subplots (a), (b), (c), (e), and (f) display the respective profiles very close to the target location. The parameters are $Q_{\perp e(i)} = 1.3 \times 10^6\,\mathrm{Wm^{-3}}$, $S_\perp = 5 \times 10^{22}\,\mathrm{m^{-3}\,s^{-1}}$, $\xi_I = 0.05$, and $R_t = 0.99$. The transition from subsonic to supersonic flow occurs just in front of the target.

where

$$\Gamma = nMc_s,$$

$$\Pi = n(T_e + T_i)(1 + M^2),$$

$$G_p(x) = 1 - \frac{1}{n_t c_{st} M_t} \int_x^{x_t} S_n dx', \tag{11}$$

$$G_m(x) = 1 - \frac{1}{n_t c_{st} M_t^2} \int_x^{x_t} \sqrt{\frac{T_e + T_i}{T_{et} + T_{it}}} M S_m dx'$$

and

$$S_n(x) = S_\perp \theta(x_x - x) + n n_n \langle \sigma v \rangle_i - n^2 \langle \sigma v \rangle_r,$$
$$S_m(x) = -n n_n \langle \sigma v \rangle_{cx} - n^2 \langle \sigma v \rangle_r, \tag{12}$$

Using the boundary condition at stagnation point, $M(0) = 0$ gives

$$n_t c_{st} M_t = \int_0^{x_t} S_n dx'.$$

The Mach number profile can then be obtained as

$$M_\pm(x) = \frac{1}{\mathcal{A}(x)}\left[1 \pm \sqrt{1 - \mathcal{A}^2(x)}\right]. \tag{13}$$

The control parameter thus obeys a condition, $\mathcal{A}^2 \leq 1$. Futhermore, it is evident from the left side of Eq. (10) that the maximum value of $\mathcal{A}$ is attained at the sonic point, where $M = 1$. However, the right side of Eq. (10) yields that the profiles of acoustic speed, particle, and momentum fluxes must be such so as to satisfy this constraint. Solving Eq. (10) involves the unknown parameter M_t, whose evaluation depends on locating the sonic point. Apparently, if the temperatures decrease rapidly with increasing x, then this sonic

point $x = x_*$ could lie upstream of the target point x_t. The location x_* can be found through the following requirements:

$$\mathcal{A}(x_*) = 1 \tag{14}$$

and

$$\left.\frac{d\mathcal{A}}{dx}\right|_{x_*} = 0. \tag{15}$$

On knowing x_*, the value of M_t can be evaluated from

$$M_t = \frac{G_p(x_*)}{G_m(x_*)} \sqrt{\frac{T_e(x_*) + T_i(x_*)}{T_{et} + T_{it}}}$$
$$+ \sqrt{\left[\frac{G_p(x_*)}{G_m(x_*)}\right]^2 \frac{T_e(x_*) + T_i(x_*)}{T_{et} + T_{it}} - \frac{1}{G_m(x_*)}}. \tag{16}$$

The total Mach number profile satisfying the boundary conditions $M(0) = 0$ and $M(x_t) \geq 1$ can then be constructed with $M = M_-$ for $0 \leq x \leq x_*$ and $M = M_+$ for $x_* \leq x \leq x_t$. A solution thus obtained is demonstrated in Fig. 3(a), where the subsonic and supersonic branches have been evaluated using Eqs. (13), (16), and the right side of Eq. (10). It must be mentioned that we find a good match between the Mach profiles calculated using the standard differential form of the motion equation, and its integral representation, expressed via Eqs. (10)–(16). The non-monotonic behaviour of $\mathcal{A}$ is seen in Fig. 3(b), and it reaches its maximum possible value of 1 very close to the target, also satisfying the condition $\partial_x \mathcal{A} \to 0$ as $\mathcal{A}^2 \to 1$.[17] To further understand the various competing mechanisms responsible for driving supersonic flows in the SOL, we investigate the gradient of control parameter $\mathcal{A}$, which can be written as
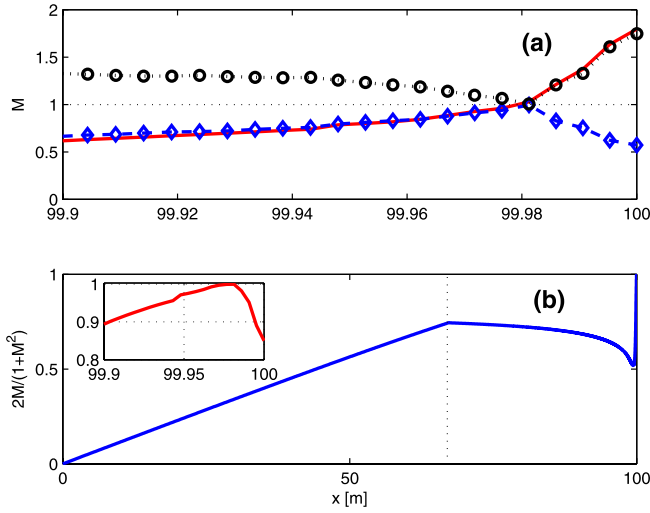
FIG. 3. Numerical profile of Mach number for detached case of Fig. 2; (a) the enlarged view of Mach number captures the position of sonic transition before the target at 100 m. Solid (red) lines represent the values obtained on simulating the differential form of fluid equations, whereas the dotted (black) and dashed (blue) lines denote the supersonic and subsonic branches, respectively. The supersonic and subsonic solutions have been evaluated by using the integral representation with Eq. (13) along with the RHS of Eqs. (10), (11), and (16). (b) Variation of control parameter $\mathcal{A}$ over the entire parallel length, and (inset) in the vicinity of sonic transition.

$$\frac{d\mathcal{A}}{dx} = \mathcal{A} \times \left[\frac{S_n}{\Gamma} - \frac{\mathcal{A}MS_m}{2\Gamma} - \frac{1}{2(T_e + T_i)} \left(\frac{T_e}{L_{T_e}} + \frac{T_i}{L_{T_i}} \right) \right] \quad (17)$$

and $L_{T_{e(i)}} = -T_{e(i)}(dT_{e(i)}/dx)^{-1}$ are the parallel temperature gradient scale lengths. It is clear that the parallel variation of $\mathcal{A}$, which at some location will satisfy Eqs. (14) and (15), is dependent on three terms forming the bracket on right side of Eq. (17). The first term is usually positive, driven by charged particle addition as well as their creation due to electron impact ionization, but can also be negative, if low

enough temperatures lead to the dominance of recombination over ionization. The second term, governed by charge exchange friction of plasma with the neutrals, is positive. The third term, which is dependent on ion and electron temperature gradients, is always negative. This indicates that in case of large temperature gradients and sufficiently low $T_{e(i)}$, the first and third term can lead to $d\mathcal{A}/dx < 0$, thus creating a situation where Eqs. (14) and (15) may be simultaneously satisfied.

In Fig. 3(b), we plotted the profile of control parameter $\mathcal{A}$ for the high density detached case, and now we examine contribution of each of the three terms constituting the bracket on the right side of Eq. (17). For clarity purpose, as shown in Fig. 4, we subdivide the parallel variation of $\mathcal{A}$ into six distinct regions. In region (i), assumed to exist from $x = 0$ to the X-point $x = x_x$, the increase in $\mathcal{A}$ implies that there is a net source of particles into the flux tube, which in our present simulation setup results almost entirely due to charged particle addition from the core. The recombination loss term is negligible due to high $T_e > 30$ eV. Due to very low neutral density, the (positive) contribution of friction can also be neglected. In this region, as can also be seen from Fig. 2(c), the temperature gradients are also small. This makes the (positive) contribution from the first term dominate the right side of Eq. (17). However, in region (ii), which starts at x_x and ends at the end of the convection/conduction zone ($x = x_c$), $\mathcal{A}$ begins to decrease. This is because the first term is now powered only by ionization of the gradually increasing neutral population. Recombination is still negligible due to relatively high T_e. The slowly mounting frictional losses are also not enough to counter the temperature gradients. The energy transport in this region is initially through convection and later by conduction due to high electron thermal conductivity. Thus, as can be seen in Fig. 4(ii), the third term prevails over the first and second term. From x_c to end of the
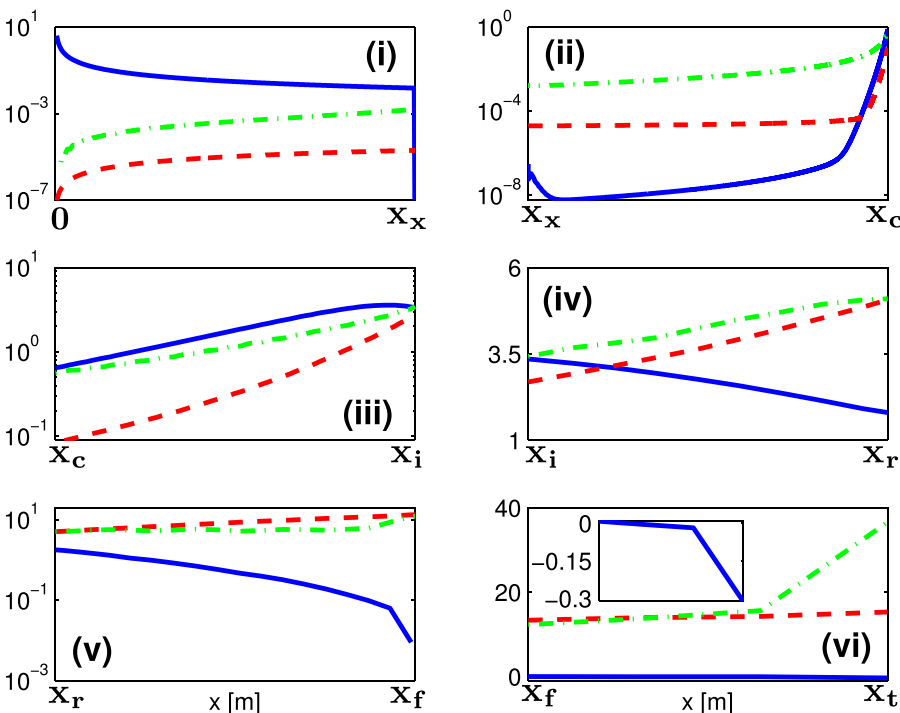

FIG. 4. Plots showing variation of the three terms constituting right side of Eq. (17). The six subplots classifying various zones have been created on the basis of monotonic increase or decrease of $\mathcal{A}$ in the respective regions. The tick labels on the x-axis x_c, x_i, x_r, x_f, mark the end of convection/conduction, ionization, radiation, and friction zones, respectively. The solid (blue) line represents the first term (S_n/Γ), while the dashed (red) line shows the second term ($-\mathcal{A}MS_m/\Gamma$), and the dashed-dotted (green) line denotes the third term $-[2(T_e + T_i)]^{-1}d(T_e + T_i)/dx$. Inset in subplot (vi) shows the first term becoming negative near the target.

ionization region ($x = x_i$), which forms region (iii), the value of $\mathcal{A}$ rises again. It stems from the first term becoming dominant due to a spurt in ionization of the ever increasing population of recycling neutrals. In this region, the temperature also drops leisurely from ~20 eV to ~10 eV, but it creates conditions that are amenable for the increase in radiative losses, which rapidly cool the plasma. This is because for carbon impurities considered here, the radiative loss peaks at $T_e \sim 10$ eV. In region (iv), which spans from x_i till the end of radiation zone ($x = x_r$), T_e drops below the ionization threshold value of ~5 eV. Thus particle creation by ionization decreases, and frictional losses are also few due to relatively lower neutral densities, inspite of a decline in ionization. This allows the temperature gradients formed, to dominate. Next, in region (v) which runs from x_r upto the end of frictional loss zone ($x = x_f$), with T_e in the range of 2–5 eV, the second term, i.e., the loss of momentum due to charge exchange friction of plasma ions with neutrals is comparatively stronger than the other two terms, yielding an increase in $\mathcal{A}$, pushing it all the way to its maximum attainable value of unity. This implies the Mach number M reaches the sonic point. Finally, in region (vi), which exists from the end of friction zone x_f to the target plate x_t, the control parameter begins to decrease. This is brought about by very low temperatures $T_e < 2$ eV, which facilitates the takeover of ionization by recombination, thereby making the first term negative as well. Notice that although $d\mathcal{A}/dx$ changes sign in going from one region to another, thereby satisfying the condition given by Eq. (15), we do not observe transition to supersonic flows in all the regions, except one. This is simply because the other condition, given by Eq. (14), is not simultaneously fulfilled.

It has also been noted that the temperature for which L_T becomes smaller than the plasma parallel mean free path for ionization L_i is a key parameter to generate supersonic flows in detached plasmas.[17] Here, $L_i = \frac{\sqrt{kT_i}}{\sqrt{m_i}(n\langle\sigma v\rangle_i)}$; and since $T_e \approx T_i$ in a detached case, we have $L_T \equiv L_{T_e} \approx L_{T_i}$. Thus, as can be seen from Fig. 5, we find that at $T_e \sim 3.5$ eV, L_i becomes larger than L_T. An almost similar value explaining the sonic transition was found in Ref. 35, and it has also been obtained using simple analytical arguments by Harbour and Loarte.[38]

B. Attached

We now turn to examine development of steady supersonic flows in case of lower density and higher target temperature plasmas.[17] It has been shown, particularly in the framework of a parallel to the field lines 1D model that, this so-called attached regime can be accessed by increasing the ratio of power and particle volume source ($Q_\perp/S_\perp$), coming from the core to the SOL region.[36] In the present case, keeping $S_\perp$ fixed, we choose to increase $Q_\perp$ and obtain results, which are displayed in Fig. (6). Compared to the high density detached case, for this case, we increased $Q_{\perp e(i)}$ to 2×10^6 W m^{-3}, with other parameters being same, as $S_\perp = 5 \times 10^{22}$ m^{-3} s^{-1}, $\xi_I = 0.05$, and $R_t = 0.99$. This solution with high R_t corresponds to the typical high-recycling regime.
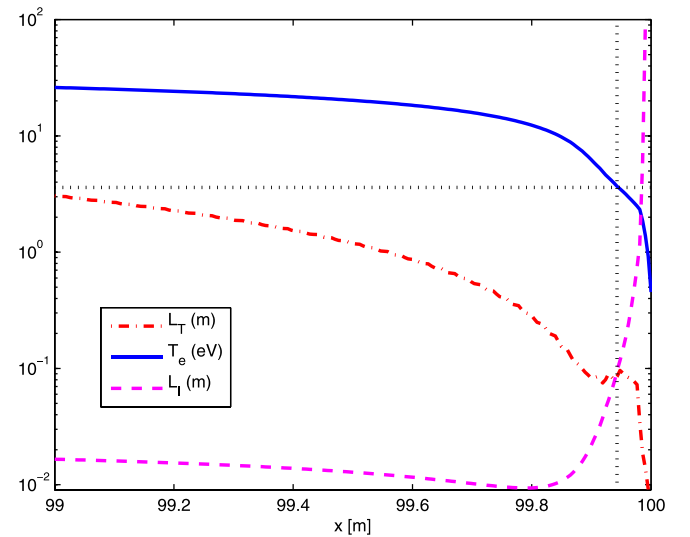

FIG. 5. A comparison of parallel lengths and plasma temperature for the high density detached case of Fig. 1. The dashed-dotted (red) line shows temperature gradient scale length (L_T); whereas the dashed (magenta) line shows the mean free path for ionization (L_i). The blue (solid) line displays the plasma temperature and the dotted (crosshair) line determines the temperature for which L_i becomes larger than L_T. In this case, the corresponding electron temperature is found to be ~3.55 eV.

Curiously, keeping all other parameters same, as used to obtain the high-recycling case in Fig. (6), but simply lowering the recycling coefficient R_t to extremely low values leads to the development of supersonic flows. These results are presented in Fig. (7), where $R_t = 0.01$. Although the upstream density and temperature values are similar in both these cases, we find that due to very low R_t and hence quite low overall and target neutral density [Fig. 7(iii)], the atomic physics effects are almost negligible. Due to such low recycling, the associated volumetric power and momentum losses are also very small. In this case, we thus find that the transition to supersonic flows is due to the decrease in density that occurs as the plasma changes from positive to an effective negative particle source.[17] As can be seen from Figs. 7(i) and 7(iv), the plasma density drops continuously inspite of moderate temperature values with $T_{e(i)} < 100$ eV. In our model, the cross-field particle transport term $S_\perp$ acts as an effective particle source till the X-point on a given field line. The remainder parallel length from x_x till the target point x_t is then bereft of an effective particle source creation, due to massive recycling loss at the target plate. From Figs. 7(v) and 6(v), the plasma particle flux (Γ) hitting the target for the supersonic flow solution is almost half of that for the subsonic high-recycling regime. However, there seems to be no difference in the total heat flux reaching the target for both these cases.

According to flow theory of a compressible fluid, supersonic flow conditions in a steady 1D *simple flow* can be reached through either of the independent driving potentials, such as (i) area change (De Laval nozzle), (ii) friction, (iii) mass addition, (iv) heat transfer, (v) chemical reactions, etc.[39] Whereas in Laval nozzle, a channel of varying cross section governs the transition between subsonic and supersonic flows, in case of SOL plasmas we find that supersonic flows can also be generated within a flux tube of constant area due to the simultaneous presence of several other
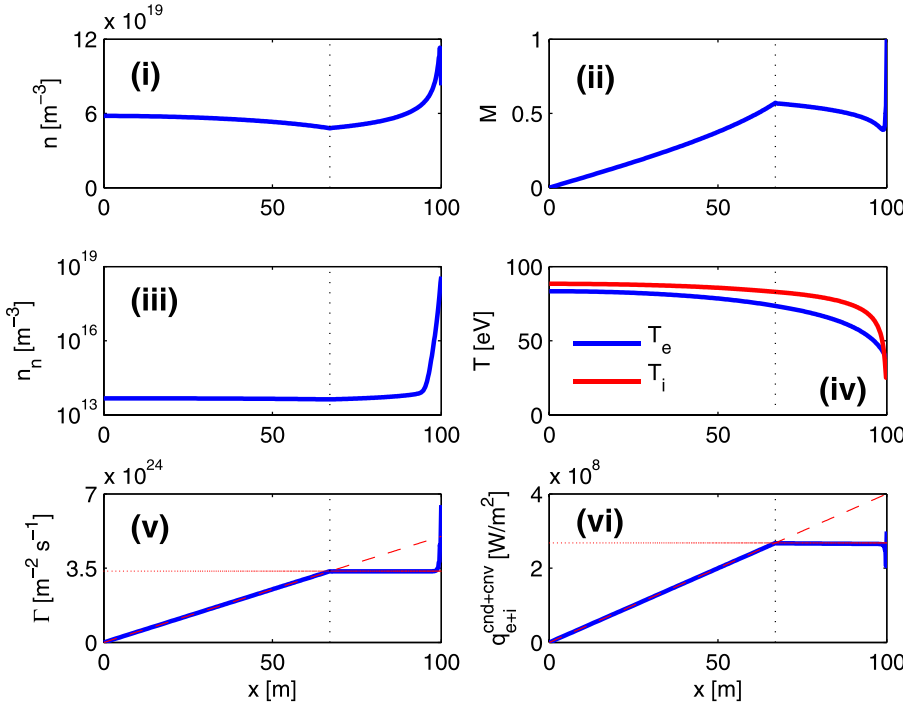
FIG. 6. Attached, high-recycling plasma flow obtained for high R_t values, obtained by only increasing the perpendicular heat entering from the core compared to the detached case in Fig. 2. The parameters chosen for this simulation run are $S_\perp = 5 \times 10^{22}\,\mathrm{m}^{-3}\,\mathrm{s}^{-1}$, $Q_{\perp e(i)} = 2 \times 10^6\,\mathrm{Wm}^{-3}$, $\xi_I = 0.05$, and $R_t = 0.99$. The thin red (dashed) lines in subplots (v) and (vi) are analytical values of particle flux (Γ) and total (conductive and convective) heat flux of electrons and ions, assuming the role of neutrals is negligible.

driving potentials. In a steady state, using Eqs. (1) and (2) and the ideal gas equation of state, changes in some generalized flow properties of a plasma can be written as

$$(1 - M^2)\frac{dM}{M} = \left[(1 + M^2)\frac{S_n dx}{\Gamma} - M^2 \frac{S_m dx}{\Gamma} \right. $$
$$\left. + \left(\frac{1 + M^2}{2}\right)\frac{d(T_e + T_i)}{T_e + T_i} \right], \quad (18a)$$

$$(1 - M^2)\frac{dp}{p} = -\left[2M^2 \frac{S_n dx}{\Gamma} - M^2 \frac{S_m dx}{\Gamma} + M^2 \frac{d(T_e + T_i)}{T_e + T_i} \right], \quad (18b)$$

where S_n and S_m are defined in Eq. (12). The last term related to temperature variation in Eqs. (18a)–(18b) can also be evaluated as follows.

Adding Eqs. (3) and (4) and after some algebra, the following relation is obtained:

$$(5 - 3M^2)\frac{d(T_e + T_i)}{T_e + T_i} = -\left[(M^4 - 2M^2 + 5)\frac{S_n dx}{\Gamma} \right.$$
$$\left. - 2M^4 \frac{S_m dx}{\Gamma} - 2(1 - M^2)\frac{Qdx - dq_c}{\Gamma(T_e + T_i)} \right], \quad (19)$$

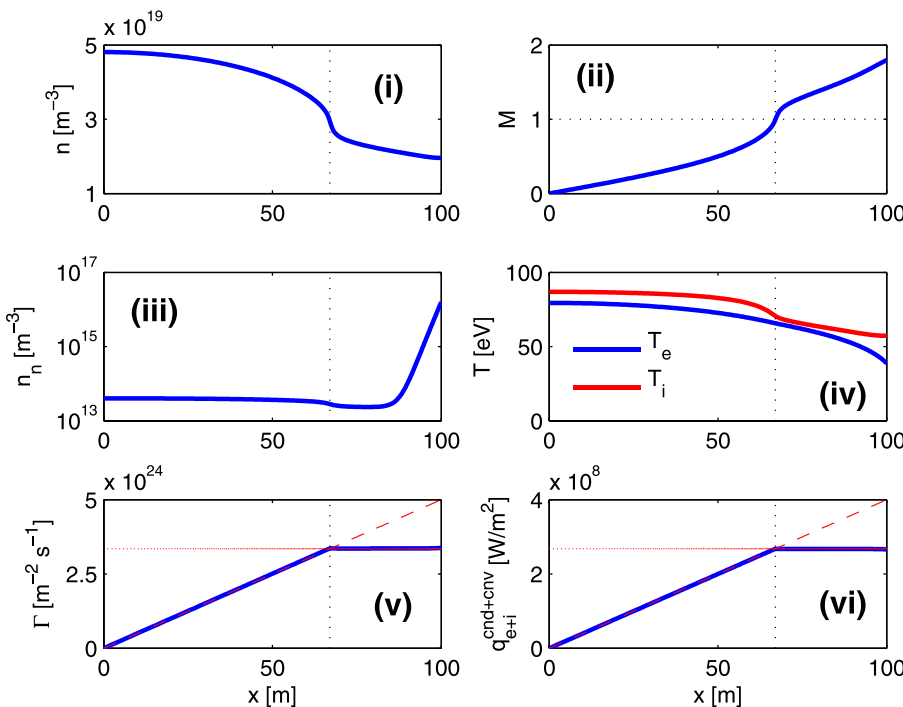where Q contains all the heat source and sink terms, while dq_c denotes the variation of total conductive heat fluxes of

FIG. 7. A typical attached supersonic plasma flow for ultra low values of R_t. Here, $R_t = 0.01$. The remaining parameters are same as used in Fig. 6. The sonic point is located at the X-point (x_x) represented by the black (dotted) vertical line, where the perpendicular heat and particles fed from the core into the parallel flux tube end.

electrons and ions. Notice that for $M = 1$, the right hand side (RHS) of Eq. (19) reduces to that of Eq. (18a) and (18b).

From Eq. (18a), it is seen that the sign of its RHS, other than whether the flow is subsonic ($M < 1$) or supersonic ($M > 1$), determines the direction of the change of M. So, if RHS is negative and the initial flow is subsonic, M decreases continuously. Similarly, if $M > 1$ initially, M continually increases. Likewise, if RHS is positive, M of an initially subsonic flow increases, whereas for an initially supersonic flow M decreases. Finally, if RHS is zero, then M remains constant. Note that the RHS can also change sign during the flow process. It is also clear from Eqs. (18a) and (18b) that the presence of friction as well as injection of mass and heat cause the Mach number M to increase and static pressure p to decrease for a subsonic flow, whereas M decreases and p increases for a supersonic flow. Conversely, removal of heat (cooling) has the opposite effect on the flow properties, i.e., when RHS is negative. Thus, it is apparent that the flow chokes at a Mach number of unity. Consequently, a continuous transition from subsonic to supersonic flow is impossible if the driving potentials are friction, mass, and heat addition. Only in the special case where RHS in Eq. (18a) is zero and $M = 1$ at the same location can such a possibility arise. This is confirmed by our numerical simulation, as shown in Fig. 8(a). The same criterion also needs to be fulfilled for continuous transition from supersonic to a subsonic flow regime.

It is apparent from Fig. 7(iii) that in the present case, we can ignore due to much lower neutral densities, the effect of ionization and friction. Taking this into account and dividing Eq. (18b) by Eq. (18a), we get

$$\frac{dp}{p} = -\left(\frac{2M^2}{1 + M^2}\right)\frac{dM}{M}. \tag{20}$$

Integrating Eq. (20) from stagnation point ($x = 0$, $p = p_0$, $M = 0$) to an arbitrary point downstream yields
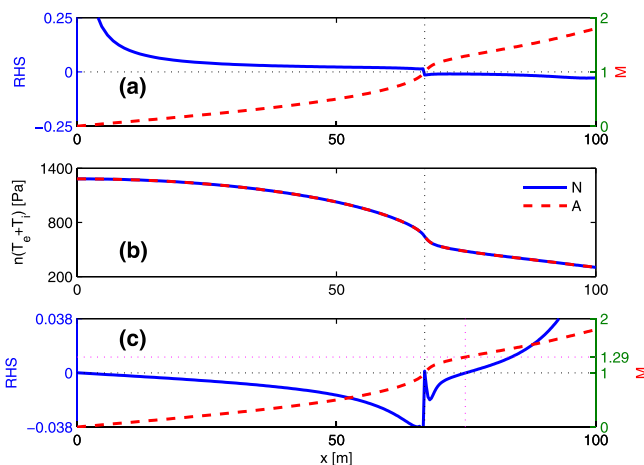
$$\frac{p}{p_0} = \frac{1}{1 + M^2}. \tag{21}$$

FIG. 8. Comparison of numerical simulation (blue solid) with the analytical (red broken) solutions for the steady state supersonic solution shown in Fig. 7. Subplots (a), (b), and (c) compare the numerical solution with Eqs. (18a), (21), and (19), respectively.

Here, p_0 is the stagnation point value of pressure. The simulated static total pressure variation is compared with that predicted by the 1D generalized flow model as shown in Fig. 8(b). An excellent agreement is obtained with the predicted analytic behaviour. In agreement with real gases, we also find that the pressure ratio p/p_0 to be approximately one-half at the point where flow changes from subsonic to supersonic, i.e., near the X-point. An additional check can be also be conducted by using Eq. (19). If the total temperature variation has to remain finite throughout, then the RHS in Eq. (19) should vanish at Mach number $M_* = \sqrt{5/3}$. This is plotted in Fig. 8(c), and it matches the expected behaviour. In Fig. 8(c), the RHS of Eq. (19) vanishes at two locations $M = 1$ and $M = M_*$, satisfying both the criteria noted above. It also changes sign before and after M_*, as both T_e and T_i decrease continuously along the entire length [see Fig. 7(iv)].

Akin to the standard supersonic nozzle, the fluid flow increases in velocity till the X-point, chokes sonic at the X-point, then expands outward supersonically, as seen from Fig. 7(ii). Since the simulated results demonstrate a continuous transition to supersonic flows, it implies that the RHS of Eq. (18a) changes from positive to negative. Note that when the RHS passes through zero and if $M = 1$ simultaneously, then two possibilities exist.[39] The flow may proceed either subsonically or supersonically. This outcome depends on conditions at the boundary downstream. Basically, if the pressure of the neutrals which result from the recycling of ions at the plate, and into which the plasma flows, is lower than the plasma pressure, then the flow remains supersonic. If however, the neutral density/pressure is high enough due to high recycling, then even a supersonic flow will be subjected to sudden compression and a shock wave is created, which can move upstream for large enough background pressure and unchoke the flow, resulting in a fully subsonic flow. In fact in rarified gas dynamics, it has been found that shock position from the nozzle exit is proportional to $\sqrt{p_e/p_b}$, where p_e and p_b are the nozzle exit/stagnation and background pressures, respectively.[40]

An evidence of this behaviour is presented in Fig. 9. Compared to Fig. (7), we raise R_t to 0.07 and 0.16, with all other parameters being same. As expected, we find that it leads to higher target neutral density and a gas cushion is thus formed in the divertor region near the target. This results in activating the major driving potentials *viz.* friction, heat, and mass addition in this region. Due to higher neutral population, the particle creation due to electron impact ionization can go up, atleast till $T_e < 100$ eV. As the charge exchange rate coefficients are weakly dependent on T_i, the momentum losses due to ion-neutral friction can also mount. However, in addition to these two mechanisms which can drive a supersonic flow toward $M = 1$, electron and ion energy losses due to ionization and charge exchange respectively, would tend to drive the flow away from $M = 1$. The effect of this competition can be gauged from the Mach number profile [Fig. 9(ii)]. For $R_t = 0.07$, M begins to drop near the target; whereas for $R_t = 0.16$, a stationary shock wave is formed as noted above. Behind this shock wave, the plasma flows subsonically into the background. We find that
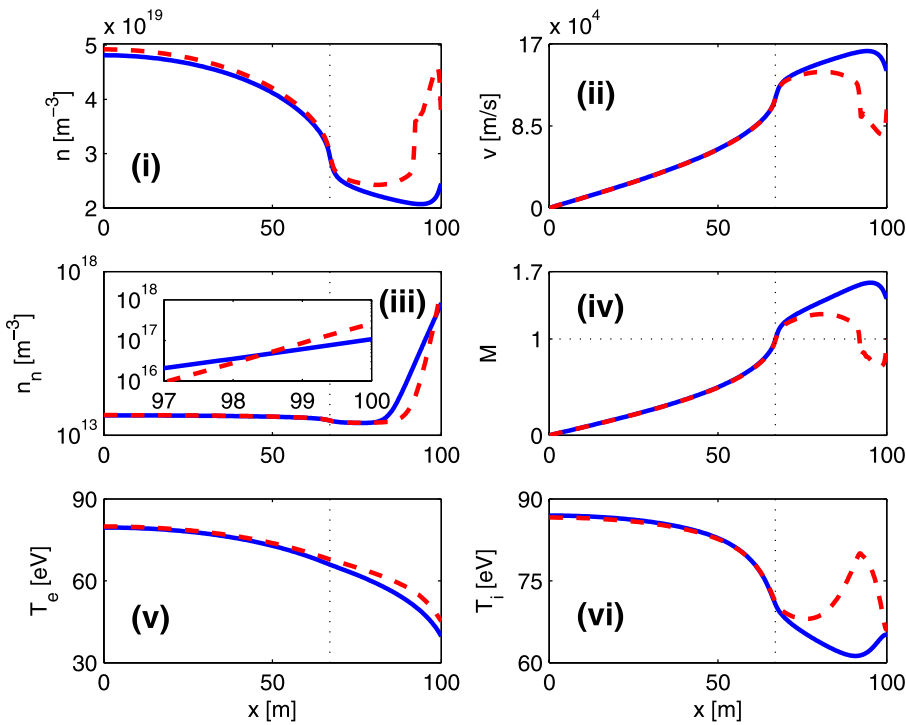
FIG. 9. Effect of increasing target recycling parameter R_t on supersonic flow. Blue (solid) and red (dashed) and curves correspond to $R_t = 0.07$ and $R_t = 0.16$, respectively. Other parameters are same as those in Fig. 6.

further increasing R_t leads to shock front approaching the X-point; and for high enough R_t, a fully subsonic solution is obtained as shown earlier in Fig. 6. Notice that the shock continues to weaken as it moves towards the X-point.

In case of shock solutions, it can be seen from Figs. 9(i), 9(ii), and 9(vi) that apart from admitting the jump in density and velocity, there is a region of smooth temperature change. The continuity of temperature across the shock front is due to the dependence of the heat flux on the temperature gradient.[41] The shock solutions are found to satisfy the Rankine-Hugoniot relations; and in accordance, we find that the density behind the shock (n_2) is higher than before the shock (n_1), with $\frac{n_2}{n_1} = \frac{(\gamma+1)M_1^2}{2+(\gamma-1)M_1^2}$, γ is the specific heat ratio.[42] It is clear that the shock wave has a two-scale structure. Apart from a shock front at $x \sim 92$ m, there also exists a much broader transition layer, where T_e also varies. The width of the sharp discontinuity is typically only a few ion-ion collision mean free paths (λ_{ii}), but the transition layer thickness is much greater than λ_{ii}.[41] Here, we find that λ_{ii} is ~ 1.7 m, comparable to the shock front width of $\lesssim 2$ m. The quasineutrality assumption also holds inside the discontinuity, as the Debye length is much smaller than λ_{ii}. There is also a considerable increase in T_i. This is because of irreversible conversion of a part of the kinetic energy of the plasma entering the compression shock into heat through dissipative mechanisms. However, due to high thermal conductivity, T_e remains smooth [Fig. 9(v)], inspite of the existence of a jump in density.

Note that the presence of such a shock in the divertor region before the X-point can also influence the penetration of impurities upstream into the main plasma. Since it is evident from Fig. 9(vi) that there is a noticeable increase in T_i behind the shock, the ion temperature gradient force can now act alongside the frictional drag and set up a barrier to

prevent further impurity incursion. From Fig. 9(ii), it can be seen that the development of large flows upstream would also help in providing the requisite frictional drag to control their movement.

Although it may appear from previous discussion that keeping all other parameters same and only adding heat, thereby raising the ratio $(Q_\perp/S_\perp)$, would lead to higher Mach number supersonic flows for ultra low values of R_t, we find that the opposite happens, as displayed in Fig. 10. The flow velocities are indeed higher till the X-point, being driven by heat addition in the subsonic range, but the local sound speed c_s rises even faster as the solutions now approach the sheath-limited regime. In this regime, the T_e and T_i values are not only higher, but have less parallel variation as well. They are also fairly decoupled due to low plasma densities. All of this cause the pressure gradient force to become quite small and despite lower frictional losses, the velocity accordingly increases extremely slowly after the X-point. The plasma is almost incompressible in this region as the density variation with temperature is quite small. This almost constant and small supersonic plasma flow after the X-point then encounters neutrals near the target region, which cause the transition to subsonic flow via a weak shock, as the discontinuities in this case are small. Increasing the said ratio further would call into question the validity of the fluid model.

C. Rarefaction

Finally, we investigate formation of supersonic flows associated with the creation of rarefaction waves in a quasi-neutral plasma. These flows are generated when some physical quantities exhibit a sudden jump, which can be realized in the perpendicular (to **B**) crossing of structures such as blobs and ELM filaments by convection. Such large-amplitude
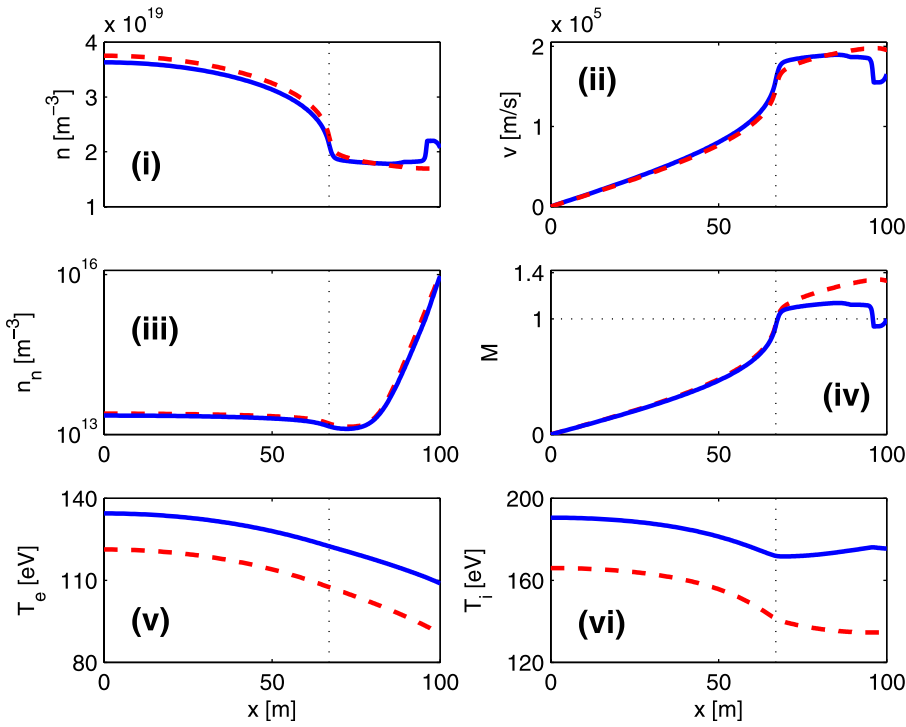
FIG. 10. Effect of high heat input on supersonic flow for ultra low R_t. Red (dashed) and blue (solid) curves correspond to $Q_{\perp e(i)} = 4 \times 10^6\,\mathrm{W/m^3}$ and $Q_{\perp e(i)} = 4.6 \times 10^6\,\mathrm{W/m^3}$, respectively. Here, $S_\perp = 5 \times 10^{22}\,\mathrm{m^{-3}\,s^{-1}}$ and $R_t = 0.01$.

quasi-periodic perturbations provide a mechanism for the substantial release of particles, heat, momentum, and parallel current in the SOL. In the present work, this cross-field transport is taken into account through a tangible increase in the values of $S_\perp$ and $Q_{\perp e(i)}$, and only one such transient event of a chain has been analyzed. The additional energy and particle sources suddenly entering the SOL flux tube from perpendicular movement of a blob-filament are simplified as a step function in time with an approximate duration and amplitude. These intermittent sources are again considered to be spatially uniform, and range from $x = 0$ to $x = x_x$. This simple assumption, though not necessary, is helped by the fact that the filaments can be quite extended along the direction of the magnetic field.[43,44]

Parallel expansion of such density bursts have been shown to generate fronts that propagate with supersonic velocities.[45] However, since blobs and ELM filaments also carry heat across the SOL, we analyze their parallel transport by including the full set of 1D fluid equations described in Sec. II. Furthermore, to incorporate the role of background plasma profiles, as initial condition we take the high-recycling steady-state solution shown in Fig. 6 and assume it to be the plasma condition before the arrival of these bursts. We consider the temporal width of the event to be $\sim 50\,\mu s$. For a clear and distinctive effect of generating supersonic flows within a rarefaction wave, the incoming perpendicular volumetric particle and heat sources of this short and over-dense burst are approximated to be $S_\perp = 1 \times 10^{25}\,\mathrm{m^{-3}\,s^{-1}}$ and $Q_{\perp e(i)} = 1 \times 10^9\,\mathrm{Wm^{-3}}$. Note that the purpose of this study is only to explore and understand the underlying physical processes and not a machine specific prediction and analysis.

In the initial development phase, as shown in Fig. 11, regions fuelled by perpendicular sources show a rapid and marked rise in the density and temperature values compared to regions downstream which are not in direct contact with the core plasma, thus creating a kind of finite parallel discontinuity between the two. As the rise stagnates after the end of the burst at $\sim 50\,\mu s$, the plasma then starts to expand, guided by thermal pressure forces into the more rarified low density part. From Fig. 11, it is evident that the plasma expansion progressively erodes the initial discontinuities through the development of a rarefaction wave. As expected and shown in Fig. 11(i), the rarefaction wave demonstrates an exponential density wave form. Concurrently, as seen in Fig. 11(ii), the Mach number also rises very fast and flow becomes supersonic. The interaction of the expanding and the ambient plasma also results in the formation of a shock. The flow returns to subsonic regime through the formation of this shock. The rarefaction wave is separated from the shock by a contact surface. We also observe that throughout the time evolution of the supersonic flow the transition point always remains at the location of the initial discontinuity,[17] which in the present case is the X-point. From Fig. 11(iv), we find that as the expansion progresses, the ion temperature drops noticeably in the regions affected. After the expansion, we observe a small region where the ion temperature rises again in the shock. This is because at the point of discontinuity, the gradients are large, and therefore the energy dissipation by heat conduction is high. Since due to high temperatures values of thermal conductivity are large, it also acts as a shock broadening mechanism,[41] leading to higher shock wave thickness in plasma, compared to those in ideal gases. Note that the rarefaction also broadens the shock wave and diminishes the gradients.

Modelling the plasma as a neutral gas is the simplest way to get basic insight into the flow field of an expanding plasma. The present simulation scenario resembles a shock tube wherein one section at high pressure is separated from a low pressure section by a diaphragm at an initial time ($t = 0$).
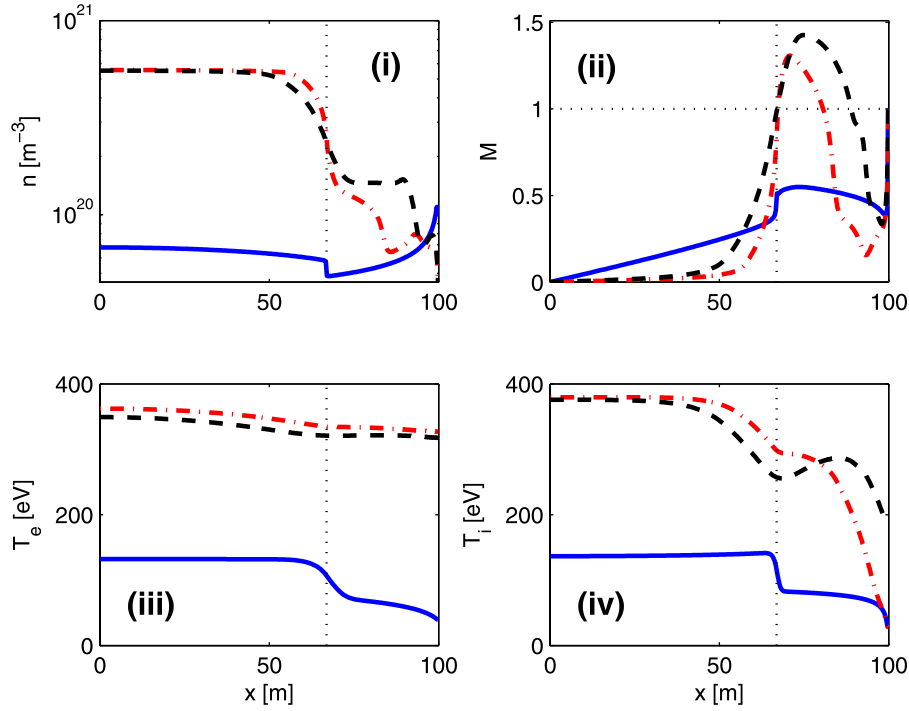
FIG. 11. Generation of supersonic flow with a rarefaction wave due to sudden burst of cross-field particle and heat. Here, the duration of this transient eruption is taken to be 50 μs. The perpendicular volumetric heat and particle densities carried by the burst is assumed to be uniform from $x=0$ to $x=x_x$ (black dotted line), with $S_\perp = 1 \times 10^{25}$ m^{-3}s^{-1} and $Q_{\perp e(i)} = 1 \times 10^9$ W/m^3. The background plasma upon which the bursty event propagates corresponds to the high-recycling attached regime shown in Fig. 5, with $R_t = 0.99$. Plotted are the development of various plasma profiles, at t $= 1 \mu$s (solid blue), and their further evolution at t $= 50 \mu$s (red dashed-dotted) and t $= 75 \mu$s (black dashed), respectively. Subplot (i) shows the formation of a rarefaction wave centered at x_x with corresponding transition to a supersonic flow. The electron temperature (T_e) in subplot (iii) remains almost constant due to high thermal conductivity. Subplot (iv) displays the ion temperature (T_i), which drops rapidly due to plasma expansion and then rises due to the unsteady shock.

Immediately, after the diaphragm is ruptured, a series of compression waves moving at supersonic speeds rapidly coalesce into a shock and propagate in the low pressure section. At the same time, a rarefaction wave originates and propagates in the opposite direction at local sound speed. As can be seen from Figs. 11(i) and 11(ii), behind the rarefaction front, the plasma density smoothly decreases while the plasma flow speed increases. The shock wave and the rarefaction wave then interact in such a manner so as to establish a common velocity and a common pressure for the gas downstream of both these waves. Once the shock is formed, it moves with a constant velocity through the medium ahead and will persist until it reaches the boundary or is caught by the rarefaction, which sweeps into the high pressure plasma and is reflected from the other boundary.

It is possible to interpret the rarefaction wave behaviour as self-similar solutions, where any functional dependence on x and t will be through the combination (x / t).[42] We now derive such an analytical solution for a quasineutral plasma and assume it to have space-time dependence through the variable $\xi = x/t$.[46] For simplicity, we ignore the effect of various sources and sinks in the governing Eqs. (1)–(4). However, it is useful to note that in the present simulation setup, the cross-field sources do not cease to exist after the passage of blob-filament like events, but continue to operate at their pre-event level since they emanate from background turbulence. Furthermore, for simplicity, we also neglect electron and ion thermal conductivities. Then adding Eqs. (3) and (4), we get the following set of equations:

$$\frac{\partial n}{\partial t} + \frac{\partial}{\partial x}(nv) = 0,$$
$$\frac{\partial v}{\partial t} + v\frac{\partial v}{\partial x} = -\frac{1}{mn}\frac{\partial}{\partial x}(p_e + p_i),$$
$$\frac{\partial}{\partial t}(p_e + p_i) + v\frac{\partial}{\partial x}(p_e + p_i) + \frac{5}{3}(p_e + p_i)\frac{\partial v}{\partial x} = 0. \quad (22)$$

After transformation, Eq. (22) yields

$$(v - \xi)n' + nv' = 0, \quad (23a)$$

$$mn(v - \xi)v' = -(p_e' + p_i'), \quad (23b)$$

$$(v - \xi)(p_e' + p_i') = -\frac{5}{3}(p_e + p_i)v', \quad (23c)$$

where primes denote differentiation with respect to ξ. Solution of Eqs. (23b) and (23c) requires

$$v = \xi \pm \sqrt{\frac{5}{3}}c_s, \quad (24)$$

where the positive sign that would give a rarefaction wave propagating toward $x=0$ is chosen. Following Ref. 46, the density variation for our case with an ambient plasma can be evaluated from Eq. (23a) as

$$n = n_0 \exp\left[-\int_{(1-\sqrt{\gamma_0})c_{s0}}^{\xi}\left(\frac{\gamma_0^{-1/2} + c_s'}{c_s}\right)d\xi\right]. \quad (25)$$
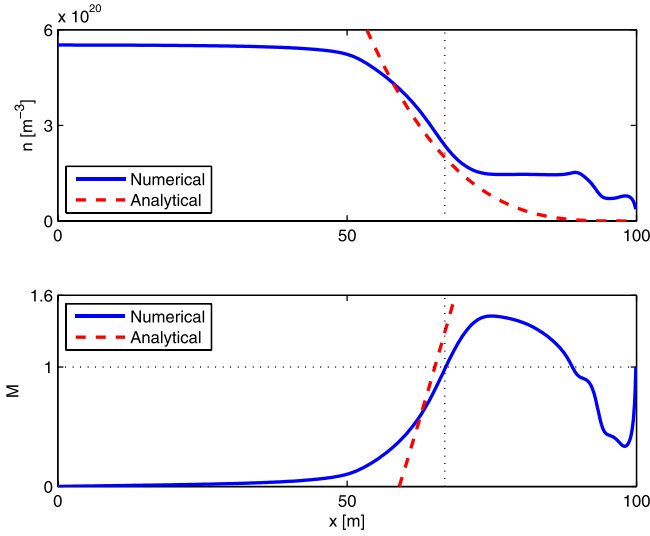
FIG. 12. Comparison of numerical (solid blue) with analytical (red dashed) result given by Eqs. (28) and (24) in the development of rarefaction waves. The top and bottom subplots show plasma density (n) and Mach number (M) number profiles at 75 μs, respectively. For the analytical solution, the initial discontinuity location is taken to be the X-point, i.e., $\xi = 0$ at $x = x_x$.

Here, $\gamma_0 = 5/3$. Using Eq. (23c), we get

$$\frac{c_s'}{c_s} = \frac{T_e' + T_i'}{2(T_e + T_i)} = \left(\frac{\gamma_0 - 1}{2}\right)\frac{n'}{n}.$$

Now substituting for n'/n from Eq. (23a) and using Eq. (24) gives

$$c_s' = -\frac{\gamma_0 - 1}{\sqrt{\gamma_0}(\gamma_0 + 1)}, \tag{26}$$

which upon integration yields

$$c_s = c_{s0} - \left[\frac{\gamma_0 - 1}{\sqrt{\gamma_0}(\gamma_0 + 1)}\right]\xi. \tag{27}$$

Substituting from Eqs. (26) and (27) into Eq. (25), the plasma density is obtained to be

$$\frac{n}{n_0} = \left[\frac{\sqrt{\gamma_0}(\gamma_0 + 1)c_{s0} - (\gamma_0 - 1)\xi}{(2\gamma_0\sqrt{\gamma_0} - \gamma_0 + 1)c_{s0}}\right]^{2/(\gamma_0 - 1)}. \tag{28}$$

The analytical results given by Eqs. (24) and (28) are compared with those obtained from the simulation at the instantaneous time of 75 μs in Fig. 12. Note that for analytical solution, we consider initial time ($t = 0$) to be at the end of the burst at 50 μs. Considering the underlying assumptions, a good match in density is obtained, validating the expansion as self-similar in nature. The main source of disagreement is due to the neglect of perpendicular source terms in deriving the analytical solution. In our case, it leads to an overestimation of velocity as given by Eq. (24), as M does not exceed unity in the numerical solutions till the X-point x_x, i.e., $\xi = 0$, due to the presence of these sources. Another probable source of disagreement could be the small numerical diffusion present in all finite-difference algorithms. The analytical solution however cannot account for the shock formation further downstream of the tail of the rarefaction wave.

As time elapses, the shock front hits the target boundary and it is reflected back and travels toward $x = 0$, as shown in Fig. 13. The density and temperature behind the reflected shock increase sharply. The solutions are also found to approximately verify the Hugoniot equation for the reflected wave,[41]

$$\frac{n_1}{n_2} = \frac{(\gamma + 1)p_1 + (\gamma - 1)p_2}{(\gamma - 1)p_1 + (\gamma + 1)p_2}, \tag{29}$$

where subscripts 1 and 2 represent quantities behind the incident and reflected wave, respectively, and $\gamma = 5/3$ is the
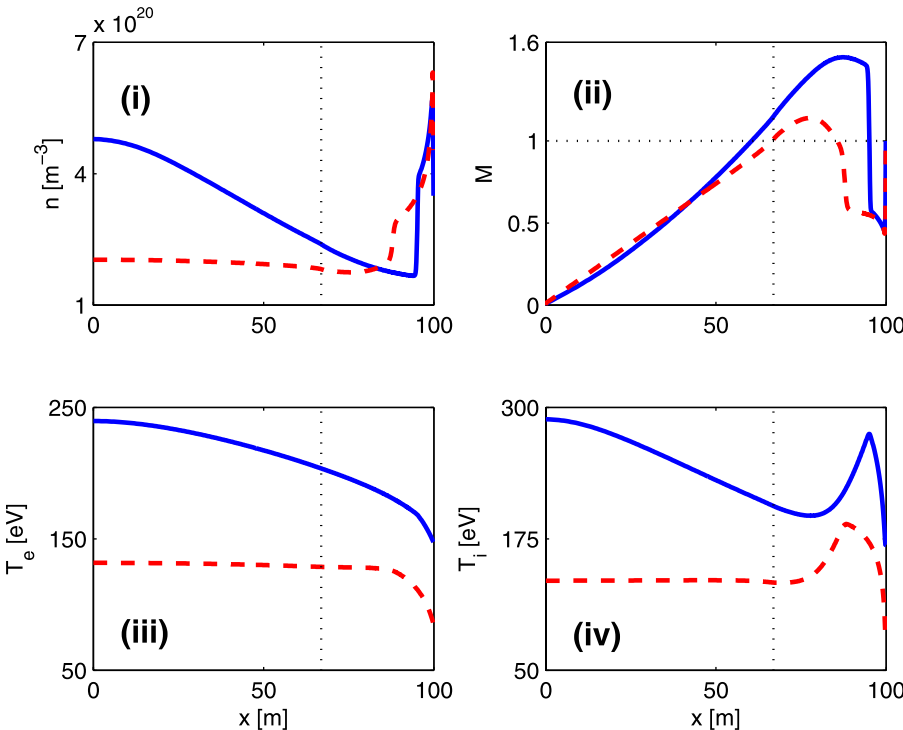

FIG. 13. Generation of reflected shock wave long time after the sudden burst of cross-field particle and heat sources shown earlier in Fig. 11. Plotted are the development of various plasma profiles, at t = 250 μs (solid blue), and its evolution at t = 550 μs (red dashed), respectively. The solutions approximately obey Eq. (29). For example, the density jump ratio (n_1/n_2) from subplot (i) at 550 μs is found to be ~0.67, while the ratio yielded by the RHS of this equation is ~0.78.
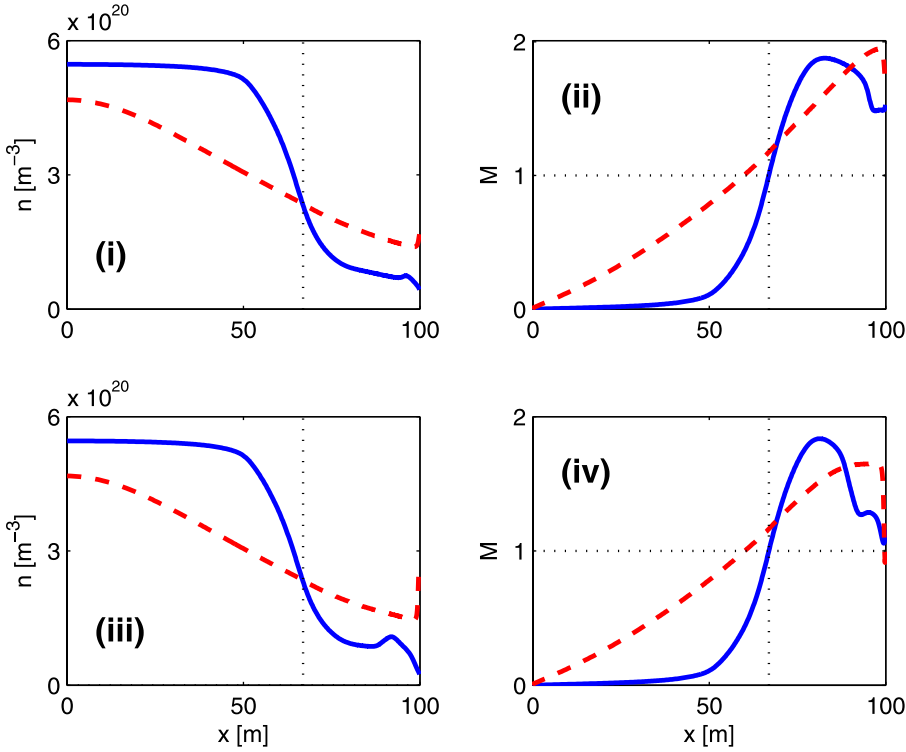
FIG. 14. Generation of a rarefaction wave without an unsteady shock for low values of target recycling parameter R_t. Plotted are the development of various plasma profiles, at $t = 75\,\mu s$ (solid blue), and its evolution at $t = 150\,\mu s$ (red dashed), respectively. Subplots (i) and (ii) depict the case for $R_t = 0.07$, while subplots (iii) and (iv) represent $R_t = 0.18$.

specific heat ratio. The reflected shock weakens as it moves towards the X-point. The solution finally relaxes back to its steady-state value existing prior to the advent of the transient. Interestingly for the same set of cross-field parameters, except a quite low target recycling coefficient R_t and its corresponding background plasma values, the shock front does not form at any instant of time. This is depicted in Fig. 14, where in subplots (i) and (ii), we chose $R_t = 0.07$, while $R_t = 0.18$ in subplots (iii) and (iv).

Finally, we would also like to point out that in a conventional shock tube, the Mach number of the shock wave M_s

depends on the pressure ratio between the two regions separated by the diaphragm. If p_1 and p_2 are pressures in the low (downstream) and high (upstream) regions, respectively, then for a perfect gas[41]

$$M_s = \sqrt{\frac{\gamma + 1}{2\gamma}\left(\frac{p_2}{p_1} - 1\right) + 1}.$$

To investigate this behaviour, we lowered the values of cross-field particle and heat sources ($S_\perp$ and $Q_{\perp e(i)}$) by half
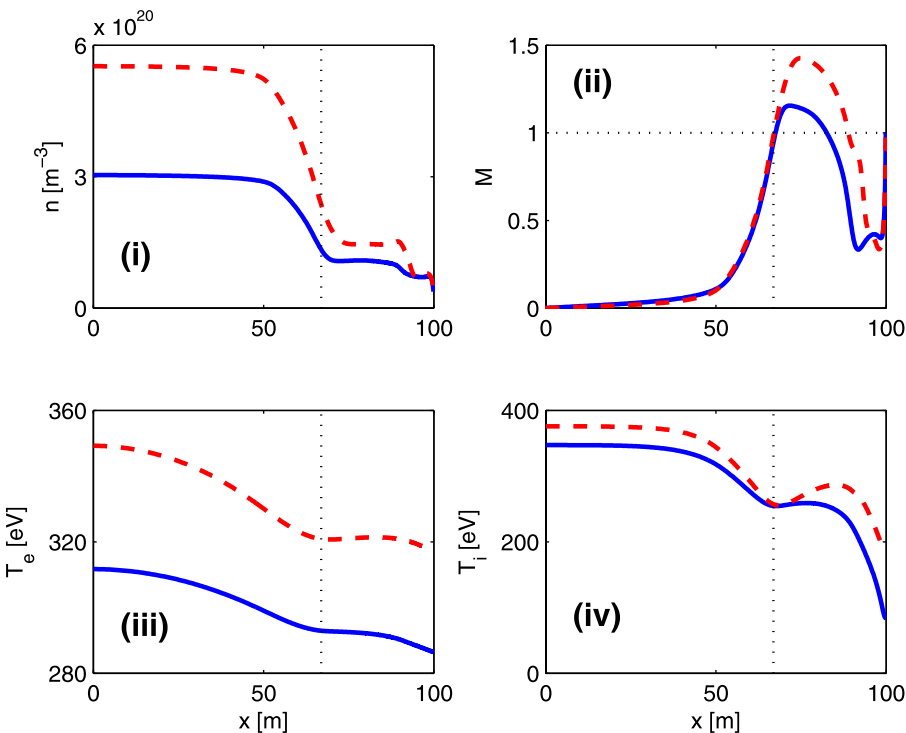

FIG. 15. Comparison of the effect of two different cross-field volumetric sources on the development of shocks. Plotted are the various plasma profiles at $75\,\mu s$ with $S_\perp = 5 \times 10^{24}\,\mathrm{m^{-3}s^{-1}}$ and $Q_{\perp e(i)} = 5 \times 10^8\,\mathrm{Wm^{-3}}$ (solid blue), and $S_\perp = 1 \times 10^{25}\,\mathrm{m^{-3}s^{-1}}$ and $Q_{\perp e(i)} = 1 \times 10^9\,\mathrm{Wm^{-3}}$ (red dashed), respectively.

with all other conditions including the ambient values being the same as in Fig. 11. So with lower values corresponding to $S_\perp = 5 \times 10^{24}\,\mathrm{m^{-3}\,s^{-1}}$ and $Q_{\perp e(i)} = 5 \times 10^8\,\mathrm{Wm^{-3}}$, it can be seen from Fig. 15(ii) that at the same instant of time ($t = 75\,\mu$s), M_s for denser and hotter bursts is indeed larger. Since the head of the centered rarefaction wave propagates into the high pressure region with local sound speed c_s, from Fig. 15(i), it can be seen that the rarefaction travels slightly farther ($c_s t$) towards $x = 0$ for higher values of $S_\perp$ and $Q_{\perp e(i)}$. Furthermore, as in neutral gas where the front thickness of a temperature profile is inversely proportional to the shock wave strength,[41] we find that a similar situation exists in the present simulation. The width of T_i around the front is smaller in case of bigger bursts as shown in Fig. 15(iv). The sharpness of the front could thus have a bearing on the entrainment of impurities via reversal of force, which is directly proportional to the magnitude of the ion temperature gradient.

IV. CONCLUSION

In summary, our work—based on comprehensive 1D SOL simulations—provide strong evidence for the existence of a bifurcation to supersonic flows in tokamak edge plasmas. We have investigated three mechanisms which submit to the possibility of such a transition to supersonic flows in a quasineutral plasma. In particular, we find that in case of steady state low divertor temperature detached plasmas, plasma particle creation and friction lead toward the sonic point; whereas, recombination and temperature gradients lead away from the sonic point. The transition to supersonic flow is found to occur right in front of the target plate. Although the particle flux reduction is found to be small, this situation would be preferable to the subsonic detached plasma regime, which can move towards the core as detachment progresses.

In case of steady state supersonic regimes associated with higher divertor temperatures and low divertor densities, particle recycling at the target plays a critical role. The effective particle source is found to be one of the key mechanism in the variation of Mach number. An attached subsonic high-recycling plasma easily transitions to supersonic flows for very low target recycling coefficient. However, we believe that if the geometrical feature of present divertor topology which gives rise to the mirror force is also taken into account, then by the virtue of its Laval nozzle like effect, the flow may get aided to become supersonic for slightly higher target recycling coefficient. In case of low-to-intermediate recycling, an interesting phenomena of a stationary shock in the divertor region is found. This can be highly useful in confining the impurities to the divertor region, due to reversal of the direction of ion temperature gradient force which otherwise normally propels them towards the core side. The impurities can thus fulfill the important role of radiating away excessive electron energy and simultaneously remain well confined as well. The exact position of the shock is found to be determined by the generation of a neutral cushion through R_t. However, one must note that for too low values of R_t, the flow remains

supersonic, and no shock wave is observed in the simulation. On the other hand, for values of $R_t \sim 1$, the flow becomes subsonic over the whole flux tube and again there is no shock wave formed.

We have also demonstrated that a transition to supersonic conditions can be achieved in rarefaction waves while maintaining quasineutrality throughout the transition. However, a time-dependence of the particle, momentum, and energy flux is required to generate such a bifurcation. Such a situation can arise during a sudden burst from the core side releasing large amounts of particle and heat originating either from a magnetohydrodynamic (MHD) eigenmode as ELMs or as blobs due to turbulence, onto the open field lines of the SOL. In the initial stages of the parallel propagation (along **B**) of this burst, its expansion into the low-pressure divertor region consists of the rarefaction wave followed by a normal shock and a subsonic relaxation zone. The plasma flow behind the rarefaction front is self-similar. For rarefaction waves, the transition location remains at the point where the initial conditions exhibit a discontinuity. The formation of an incident and reflected nonstationary shock front in this case can again provide a transient barrier against impurity penetration. Also we find that contrary to a steady state attached regime, in case of rarefaction wave creation, the shock front appears to form easily for high recycling regimes with $R_t \sim 1$. However, it is also to be noted that in both cases involving steady and non-steady shocks, restraining of impurities in the divertor region also benefits from the development of large upstream flows, which can help sweep them towards the target. Also note that the shock strength is found to be directly related to the pressure in the upstream region of the SOL. This implies that for larger eruptions of blob-filaments such as in type-I ELMs, the possibilities of creating a rarefaction wave and associated supersonic flows culminating in an unsteady shock are higher.

The present simulation uses a diffusion based model for neutrals, which should be reconsidered for long mean free paths. Using a better, preferably a Monte-Carlo model for neutrals is planned for future work. The role of many 2D effects, including drifts, detailed neutral and impurity generation and transport remains to be investigated for examining the influence of various factors, which may trigger a transition to supersonic flows. Such complete 2D simulations with target boundary condition $M_t \geq 1$ can also shed more light on the development of steady shock in case of attached supersonic regimes. The applicability of continuum approach to supersonic plasma modelling should also be analysed and validated by the comparison with the results of kinetic models and experimental data. The dynamics of blob-filaments subjected to simultaneous parallel expansion and perpendicular convection can also be a part of future study. Finally, we mention that the SOL1D solver developed and used in this study has been coupled to the integrated modelling code CRONOS, allowing a self-consistent and dynamic computation of the boundary density and temperature values at the last closed flux surface (LCFS). Demonstration and validation of this coupled simulation will be carried out in a coming paper.

ACKNOWLEDGMENTS

[1]G. F. Matthews, J. Nucl. Mater. **337–339**, 1 (2005).

[2]R. A. Pitts, J. P. Coad, D. P. Coster, G. Federici, W. Fundamenski, J. Horacek, K. Krieger, A. Kukushkin, J. Likonen, G. F. Matthews *et al.*, Plasma Phys. Controlled Fusion **47**, B303 (2005).

[3]B. LaBombard, J. E. Rice, A. E. Hubbard, J. W. Hughes, M. Greenwald, R. S. Granetz, J. H. Irby, Y. Lin, B. Lipschultz, E. S. Marmar *et al.*, Phys. Plasmas **12**, 056111 (2005).

[4]D. Moulton, Ph. Ghendrih, W. Fundamenski, G. Manfredi, and D. Tskhakaya, Plasma Phys. Controlled Fusion **55**, 085003 (2013).

[5]C. T. Chang, L. W. Jorgensen, P. Nielsen, and L. L. Lengyel, Nucl. Fusion **20**, 859 (1980).

[6]N. Singh and R. W. Schunk, J. Geophys. Res. **87**, 9154, doi:10.1029/JA087iA11p09154 (1982).

[7]N. Asakura, ITPA SOL, and Divertor Topical Group, J. Nucl. Mater. **363–365**, 41 (2007).

[8]J. P. Gunn, C. Boucher, M. Dionne, I. Ďuran, V. Fuchs, T. Loarer, I. Nanobashvili, R. Pánek, J.-Y. Pascal, F. Saint-Laurent *et al.*, J. Nucl. Mater. **363–365**, 484 (2007).

[9]A. Hatayama, H. Segawa, R. Schneider, D. P. Coster, N. Hayashi, S. Sakurai, N. Asakura, and M. Ogasawara, Nucl. Fusion **40**, 2009 (2000).

[10]B. LaBombard, J. E. Rice, A. E. Hubbard, J. W. Hughes, M. Greenwald, J. H. Irby, Y. Lin, B. Lipschultz, E. S. Marmar, C. S. Pitcher *et al.*, Nucl. Fusion **44**, 1047 (2004).

[11]N. Smick, B. LaBombard, and I. H. Hutchinson, Nucl. Fusion **53**, 023001 (2013).

[12]H. W. Müller, V. Bobkov, A. Herrmann, M. Maraschek, J. Neuhauser, V. Rohde, A. Schmid, M. Tsalas, and ASDEX Upgrade Team, J. Nucl. Mater. **363–365**, 605 (2007).

[13]E. G. Fontheim and P. M. Banks, Planet. Space Sci. **20**, 73 (1972).

[14]P. C. Stangeby, Phys. Plasmas **2**, 702 (1995).

[15]N. Tsois, C. Dorn, G. Kyriakakis, M. Markoulaki, M. Pflug, G. Schramm, P. Theodoropoulos, P. Xantopoulos, M. Weinlich, and ASDEX Upgrade Team, J. Nucl. Mater. **266–269**, 1230 (1999).

[16]O. Marchuk and M. Z. Tokar, J. Comput. Phys. **227**, 1597 (2007).

[17]P. Ghendrih, K. Bodi, H. Bufferand, G. Chiavassa, G. Ciraolo, N. Fedorczak, L. Isoardi, A. Paredes, Y. Sarazin, E. Serre *et al.*, Plasma Phys. Controlled Fusion **53**, 054019 (2011).

[18]R. Schneider, X. Bonnin, K. Borrass, D. P. Coster, H. Kastelewicz, D. Reiter, V. A. Rozhansky, and B. J. Braams, Contrib. Plasma Phys. **46**, 3 (2006).

[19]T. D. Rognlien, J. L. Milovich, M. E. Rensink, and G. D. Porter, J. Nucl. Mater. **196–198**, 347 (1992).

[20]D. Reiter, J. Nucl. Mater. **196–198**, 80 (1992).

[21]R. Simonini, G. Corrigan, G. Radford, J. Spence, and A. Taroni, Contrib. Plasma Phys. **34**, 368 (1994).

[22]J. F. Artaud, V. Basiuk, F. Imbeaux, M. Schneider, J. Garcia, G. Giruzzi, P. Huynh, T. Aniel, F. Albajar, J. M. Ané *et al.*, Nucl. Fusion **50**, 043001 (2010).

[23]D. A. D'Ippolito, J. R. Myra, and S. J. Zweben, Phys. Plasmas **18**, 060501 (2011).

[24]E. Havlíčková, W. Fundamenski, M. Wischmeier, G. Fishpool, and A. W. Morris, Plasma Phys. Controlled Fusion **56**, 075008 (2014).

[25]M. Z. Tokar, Plasma Phys. Controlled Fusion **35**, 1119 (1993).

[26]S. Nakazawa, N. Nakajima, M. Okamoto, and N. Ohyabu, Plasma Phys. Controlled Fusion **42**, 401 (2000).

[27]D. A. Knoll, P. R. McHugh, S. I. Krasheninnikov, and D. J. Sigmar, Phys. Plasmas **3**, 293 (1996).

[28]P. J. Roache, *Fundamentals of Computational Fluid Dynamics* (Hermosa, 1998).

[29]R. Goswami, "A fast and smoothly converging tokamak edge fluid code," Comp. Phy. Commun. (submitted).

[30]A. Loarte, B. Lipschultz, A. S. Kukushkin, G. F. Matthews, P. C. Stangeby, N. Asakura, G. F. Counsell, G. Federici, A. Kallenbach, K. Krieger *et al.*, Nucl. Fusion **47**, S203 (2007).

[31]B. Lipschultz, X. Bonnin, G. F. Counsell, A. Kallenbach, A. S. Kukushkin, K. Krieger, A. Leonard, A. Loarte, R. Neu, R. A. Pitts *et al.*, Nucl. Fusion **47**, 1189 (2007).

[32]P. C. Stangeby, *The Plasma Boundary of Magnetic Fusion Devices* (Institute of Physics Publishing, Bristol, 2000).

[33]K. Hoshino, K. Shimizu, T. Takizuka, N. Asakura, and T. Nakano, J. Nucl. Mater. **415**, S549 (2011).

[34]Ph. Ghendrih, Phys. Plasmas **1**, 1929 (1994).

[35]A. V. Nedospasov and M. Z. Tokar, in *IAEA Technical Committee Meeting on Fusion Reactor Technology* (Yalta, USSR, 1986), IAEA-TC-392.3/44, p. 113.

[36]R. Goswami, P. Kaw, M. Warrier, R. Singh, and S. Deshpande, Phys. Plasmas **8**, 857 (2001).

[37]M. Greenwald, Plasma Phys. Controlled Fusion **44**, R27 (2002).

[38]P. J. Harbour and A. Loarte, Contrib. Plasma Phys. **34**, 312 (1994).

[39]M. J. Zucrow and J. D. Hoffman, *Gas Dynamics* (John Wiley & Sons, 1976).

[40]W. S. Young, Phys. Fluids **18**, 1421 (1975).

[41]Ya. B. Zel'dovich and Yu. P. Raizer, *Physics of Shock Waves and High-Temperature Hydrodynamic Phenomena* (Academic Press, 1967).

[42]L. D. Landau and E. M. Lifshitz, *Fluid Mechanics*, 2nd ed. (Butterworth-Heinemann, 2000).

[43]A. Kirk, B. Koch, R. Scannell, H. R. Wilson, G. Counsell, J. Dowling, A. Herrmann, R. Martin, M. Walsh, and MAST Team, Phys. Rev. Lett. **96**, 185001 (2006).

[44]N. Fedorczak, J. P. Gunn, Ph. Ghendrih, G. Ciraolo, H. Bufferand, L. Isoardi, P. Tamain, and P. Monier-Garbet, J. Nucl. Mater. **415**, S467 (2011).

[45]G. Chiavassa, H. Bufferand, G. Ciraolo, Ph. Ghendrih, H. Guillard, L. Isoardi, A. Paredes, F. Schwander, E. Serre, and P. Tamain, J. Nucl. Mater **415**, S613 (2011).

[46]J. Denavit, Phys. Fluids **22**, 1384 (1979).